Storm morphology and rainfall characteristics of TRMM precipitation features

STEPHEN W. NESBITT[1], ROBERT CIFELLI, AND STEVEN A. RUTLEDGE

Department of Atmospheric Science,
Colorado State University,
Fort Collins, Colorado

Submitted to *Monthly Weather Review*
12 July 2005

Revised
21 December 2005

Accepted
28 December 2005

[1] Corresponding author address: Dr. Stephen W. Nesbitt, Department of Atmospheric Science, Colorado State University, Fort Collins, CO 80523-1371.
E-mail: snesbitt@radarmet.atmos.colostate.edu

ABSTRACT

Tropical Rainfall Measuring Mission (TRMM) Precipitation Radar (PR), TRMM Microwave Imager (TMI) and Visible and Infrared Scanner (VIRS) observations within the Precipitation Feature (PF) database have been analyzed to examine regional variability in rain area and maximum horizontal extent of rainfall features, and role of storm morphology on rainfall production (and thus modes where vertically integrated heating occurs). Particular attention is focused on the sampling geometry of the PR and the resulting impact on PF statistics across the global Tropics. It was found that 9 percent of rain features extend to the edge of the PR swath, with edge features contributing 42 percent of total rainfall. However, the area (maximum dimension) distribution of PR features is similar to the wider-swath TMI up until a truncation point of nearly 30 000 km^2 (250 km), so a large portion of the feature size spectrum may be examined using the PR as with past ground-based studies.

This study finds distinct differences in land and ocean storm morphology characteristics, which lead to important differences in rainfall modes regionally. A larger fraction of rainfall comes from more horizontally and vertically developed PFs over land than ocean due to the lack of shallow precipitation in both relative and absolute frequency of occurrence, with a tri-modal distribution of rainfall contribution versus feature height observed over the ocean. Mesoscale Convective Systems (MCSs) are found to be responsible for up to 90 percent of rainfall in selected land regions. Tropics-wide, MCSs are responsible for more than 50 percent of rainfall in almost all regions with average annual rainfall exceeding 3 mm dy^{-1}. Characteristic variability in the contribution of rainfall by feature type is shown over land and ocean, which suggests new approaches for improved convective parameterizations.

1. Introduction

The large-scale atmospheric response to radiative forcing, latent heating, and momentum transport by precipitating systems in a regional sense depends wholly on the systems' structure in both the horizontal and vertical dimension. Global circulation models (GCMs) that aim to simulate precipitation and its large-scale effects on the environment, either through cumulus parameterizations (Arakawa 2004) or through cloud-resolving 'superparameterizations' (Grabowski 2002, 2003) must accurately simulate the spectrum of precipitating system characteristics the models aim to represent.

Many studies have used a number of remote sensing platforms to quantify the populations, characteristics, and organizational structure of cloud and rainfall systems regionally and throughout the Tropics. Statistics of ground-based radar reflectivity fields collected during tropical field campaigns have been analyzed in a number of studies (Biondini 1976; López 1976, 1977, 1978; Houze and Cheng 1978; Houze and Betts 1981; Keenan and Carbone 1992; DeMott and Rutledge 1998; Rickenbach and Rutledge 1998; Johnson et al. 1999; Cetrone and Houze 2006). Many of these studies have shown a lognormal size distribution of both radar echo top height (ETH) and echo maximum dimension (FMD). However, the range of ground-based radar (~150 km) and practical deployment time (1-3 months) limits the size and climatic representativeness of features, respectively, observed by the radar in a given location. Accordingly, a more global view provided by satellites is desirable when examining the large-scale variability in convective system characteristics.

Infrared brightness temperatures retrieved from geostationary satellite platforms have been used extensively to count and characterize populations of cold cloud clusters,

mainly due to the platform's large areal sample and high temporal resolution. Williams and Houze (1987), Mapes (1993), Mapes and Houze (1993), and Machado and Rossow (1993) each demonstrated the importance of Tropical mesoscale cloud clusters in contributing to total convective cloudiness. Nevertheless, since the relationship between cold cloud, precipitation, and latent heating is poorly understood (Rickenbach 1999), more direct proxies are necessary to quantify the characteristics and large-scale effects of Tropical precipitating systems.

The launch of the Tropical Rainfall Measuring Mission (TRMM) satellite (Simpson et al. 1988; Kummerow et al. 1998) on 28 November 1997 has initiated an era of greatly expanded quantitative description of Tropical precipitation systems. Largely through use of data from the TRMM Precipitation Radar (PR), allowing 3-D retrievals of radar reflectivity and precipitation rate, many works have examined, mainly separately, the horizontal and vertical structure of precipitating systems within the ±35° inclination orbit of TRMM. Combined with TRMM Microwave Imager (TMI) and Lightning Imaging Sensor (LIS) observations, Nesbitt et al. (2000), Toracinta et al. (2001), and Cecil et al. (2005) examined the radar reflectivity, 85 GHz ice scattering, and lightning flash rate characteristics of precipitation features (PFs, or areas of contiguous near-surface radar echo and 85 GHz ice scattering). These studies contrasted less convectively intense PFs over ocean regions with more convectively intense PFs over land regions as evidenced by differences in PR ETHs, TMI minimum 85 GHz brightness temperatures, and lightning flash rates. Studies have emphasized various portions of the convective intensity spectrum as well in their role in Tropical water budgets. Short and Nakamura (2000) highlight the high frequency of occurrence of shallow precipitation over the Tropical

oceans, while Takayabu (2002) showed the variation of the entire intensity spectrum of PR profiles. Petersen and Rutledge (2001) emphasized the regional direct relationship between increased ice and supercooled liquid water contents in convectively intense storms (as evidenced by increased frequency of higher PR reflectivity values at greater heights) and LIS flash rates, owed to strong regional differences in the vertical structure of convection. Schumacher and Houze (2003a) examined the variability of bulk TRMM PR stratiform-rain fractions within the deep Tropics, finding strong regional gradients in this quantity. This finding implied significant differences in the large-scale response to precipitation among Tropical regions (Schumacher et al. 2004). However, hitherto the horizontal structure of precipitation systems has not been investigated with TRMM Tropics-wide, particularly with emphasis on how convective system organization impacts regional rainfall production.

This study aims to provide an important link between the vertical and horizontal structure of PFs and their rainfall characteristics through analysis using the "version 6" TRMM Precipitation Feature Database (Nesbitt and Zipser 2003), which incorporates not only PR and TMI observations, but also those from the Visible Infrared Radiation Scanner (VIRS) and LIS (the latter is not used in this study). The PF Database is used to illustrate rainfall system morphology Tropicswide, highlighting regional differences in the organization of rainfall systems. In addition, this study examines the relationship of both horizontal size and proxies for convective intensity (vertical structure) to regional rainfall budgets. This study represents a preliminary step in model evaluation in putting forth an observational dataset that can be used to directly evaluate the performance of

cloud-resolving models or GCM superparameterizations in representing rainfall system variability.

2. Data

1) The TRMM satellite

The reader is referred to Kummerow et al. (1998) for detailed information on the specifications of the TRMM PR, TMI, and VIRS instruments[2]. Briefly, the PR is a K_u-band (2.2 cm wavelength) radar that has 4.3 (0.25) km resolution in the horizontal (vertical) at nadir, yielding a 215-km swath in the horizontal and range bins from just below the earth ellipsoid to nominally 20 km MSL. The PR is regularly calibrated both internally and externally and maintains stability to within ±1 dB. Attenuation-correction and precipitation estimation is provided by the version 6 2A25 algorithm (Iguchi et al. 2000), whereby a "hybrid" attenuation correction method blends a surface reference technique and a Hitchfield-Bordan (1954) reflectivity-attenuation relationship to correct reflectivity, adjust DSD parameters based on estimated attenuation, and estimate rainfall using a *Z*-*R* technique. In version 6, gaseous and cloud water attenuation is now taken into account, while there is increased reliance on the surface reference technique for rain attenuation correction relative to version 5 (T. Iguchi, personal communication). The 2A23 convective-stratiform separation algorithm is used to identify rain type; version 6 of the algorithm now flags shallow, isolated rain as convective (Schumacher and Houze 2003b).

The TMI is an elliptically scanning 9-channel dual-polarization passive microwave radiometer with a 760-km swath width with five frequencies spanning 10 to 85 GHz. At

[2] This study uses pre-boost version 6 TRMM products. More details about the TRMM algorithms may be found at http://tsdis.gsfc.nasa.gov.

85 GHz, the depression of brightness temperatures is accomplished by scattering due to optical depths of precipitation-sized ice particles within the instrument footprint (5 × 7 km for TMI, with 14 km between successive scans). To remove the effects of varying surface emissivity, PCT (Spencer et al. 1989) is calculated from the version 6 1B11 algorithm 85-GHz horizontally- and vertically-polarized brightness temperatures, denoted as T_{b_H} and T_{b_V}, respectively:

$$\mathrm{PCT} = \frac{\beta T_{b_H} - T_{b_V}}{\beta - 1}. \tag{1}$$

with β calculated to be 0.45 at 85 GHz.

The surface rain field is used from the TMI 2A12 algorithm herein in a qualitative sense (i.e. identifying areas with rain > 0 mm h^{-1}) to examine the statistics of 2A12 indicated rain areas that extend beyond the PR swath into the TMI swath. The reader is referred to Kummerow et al. (2001) for information on the 2A12 rain algorithm. Note that the 2A12 rainfall algorithm relies on fundamentally different retrieval physics over ocean (emission) than land (scattering), sensitivities, and resolution and beamfilling effects (the 10 GHz emission channel, used only over ocean, has an field of view of nearly 3 600 km^2, versus 35km^2 at the 85 GHz ice scattering channel, which is used in the over-land retrieval). Thus, there exist distinctly different retrieval characteristics over the two surfaces, making quantitative regional comparisons of TMI rain areas difficult (Nesbitt et al. 2004).

VIRS is a 5-channel cross-track visible-infrared scanning radiometer, with a ±45° scan yielding a 720-km swath width. The spatial resolution of the measurements is 2.11 km at nadir.

2) The version 6 PF algorithm

The philosophy behind the "version 6" TRMM PF database is similar to the "version 5" database outlined in Nesbitt et al. (2000) and Nesbitt and Zipser (2003). TMI pixels are matched to PR pixels using a nearest neighbor approach. Once the matching is performed, the statistical properties of contiguous areas (including corner pixels) of PR near-surface reflectivity ≥ 20 dBZ or TMI 85-GHz PCT ≤ 250 K are compiled within the PR swath. The minimum number of pixels in each PF is set to one versus four pixels as in works following the methodology laid out in Nesbitt et al. (2000), as noise, clutter, and sidelobe contamination are largely non-existent in version 6 2A25 above 20 dBZ. In addition, at least one pixel must meet the PR criteria (as an attempt to ensure at least some near-surface rainfall) in each PF, which is a also departure from previous works. This change in thresholds increases the number of PFs, area covered by PFs, and rainfall volume from PFs in the version 6 database by a factor of 3.26, 1.10, and 1.05 compared to the definition used in the version 5 studies, respectively. In addition, an improved PF snow screen has been implemented to flag features over radiometrically cold surfaces (see Nesbitt et al. 2004 for discussion of this issue) as in Cecil et al. (2005), which ensures physical consistency between areal coverage of cold brightness temperatures and surface precipitation as estimated by the PR. Separate, but similar PF statistics of the TMI 2A12 surface rain pixels with rain rate > 0 mm h^{-1} are kept for features within the wider TMI swath.

In addition to PR and TMI data, the version 6 PF database includes VIRS 11.7 μm brightness temperatures, which are interpolated from the VIRS native grid to the PR grid. Lightning Imaging Sensor (LIS) data are also included in the database, although not employed in this study.

This study uses three years of PF data including the calendar years of 1998, 1999, and 2000. PF characteristics are tabulated storm by storm, assigned to be over land or over ocean based upon their centroid location compared with a 0.5° resolution land-ocean mask. Gridded composites also generated at $(2.5°)^2$ resolution, with PFs gridded according to their centroid location.

3. Determining PF horizontal dimension

Fig. 1 shows two examples where PFs have been identified within the matched version 6 data. Panels (a) and (c) shows VIRS 11 μm T_bs and 85 GHz PCTs for an ensemble of storms over the South Pacific on different dates, corresponding PR near-surface reflectivities and LIS lightning flash locations appear in panels (b) and (d). The near surface reflectivity shows a much different picture of the presumed rainfall and net integrated latent heating compared to the IR cloud top and 85 GHz ice scattering measurements in both scenes. The VIRS and TMI observations suggest larger, more uniform coverage and intensity of rainfall compared with the PR observations, which are able to better delineate heavy convective rainfall from stratiform rainfall. Thus, this study uses the PR estimates of feature size motivated by the fact that it is presumed to be the most direct estimate of rainfall coverage; however, TMI rain areas are compared with PR areas to evaluate the effects of varying swath width.

The horizontal dimension of PFs is herein characterized using two methods. The number of raining PR pixels is counted and multiplied by the effective field of view of the instrument giving the raining area of each feature. In addition, an ellipse-fitting technique is employed whereby the major and minor axis lengths (a and b) are calculated from the mass distribution tensor Eigenvalues of the raining points within each feature (Medioni et al. 2000). Twice the major axis of the ellipse is recorded as the feature's maximum dimension (FMD).

Fig. 2 shows a density plot of the rain area of each PF versus its ellipse fit area (calculated by πab) on a log-log axis. At small feature areas (up to 100 km^2), the rain area and ellipse areas tend to be very similar. However, at areas > 100 km^2, the ellipse areas tend to be larger than the rain areas, with the modal ellipse area value being 76% larger for features > 100 km^2. This shows that the rain area of the ellipse fit feature is generally smaller than the fitted ellipse area since the ellipse fit contains both raining and non-raining areas.

Fig. 3 (a) and (b) show cumulative distribution functions (CDFs) of feature rain area (a) and FMD (b) for all features (solid line), and separately features that do not intersect the edge of the PR swath (solid line), and features that do intersect the edge (dashed line). As shown in panel a, 41% of features are 1 pixel (17.92 km^2) in area; 99.2% have areas less than 1000 km^2. The maximum PF area observed was 322883 km^2. In terms of FMD (in panel b), the same 41% of features which have 1 pixel areas have FMDs of 4.23 km ($\sqrt{17.92\ \text{km}^2}$); 98.5% of features have FMDs less than 100 km. The maximum FMD observed was 3782 km. When non-edge features are considered, their areal distributions and FMD are very similar in shape to the entire feature distribution, but is shifted slightly

to smaller sizes while edge features tend to be significantly larger in area and FMD than the distribution of all features. In all, 9% of features from the 3-yr database intersect the edge.

Panels (c) and (d) of Fig. 3 show the fraction of features hitting the edge as a function of feature area (c) and FMD (d). The probability of a feature intersecting the edge of the swath increases with feature size until nearly all PFs intersect the edge at the upper end of the distribution. Half the features intersect the edge of the PR swath at an area (FMD) of 9332 km^2 (223 km).

Since the feature size distribution varies regionally, the impact of edge features on the statistics of the feature size distribution will accordingly vary. Fig. 4 shows (a) the number fraction and (b) rainfall fraction of features intersecting the edge of the swath. Both quantities are maximized in the ITCZ and in mid-latitude areas. The number fraction of edge features is higher over land than ocean because of a lower fraction of smaller features over land (which have a higher lower probability of intersecting the swath edge). In all, the 9% of features that intersect the edge of the PR swath contribute 42% of rainfall to the PR estimates. The rainfall fraction of edge features is highest at mid-latitudes (over 60% in many areas) where the PR swath is undoubtedly slicing elongated frontal PFs, and lowest in the subtropical highs where PFs are small and less than 10% of rainfall occurs in edge features.

a) Comparisons of PR PF size distributions with other estimates

To examine the impact of the PR's relatively narrow swath width on precipitation feature size characteristics, the PR-swath derived features were compared with TMI-derived feature areas (with a swath width 3.5 times the PR's) within the TMI surface rain

field (rain rate > 0 mm h^{-1}) for the same time period as the PR results. Fig. 5 shows CDFs of PF area (solid lines) and the PF area-weighted probability density function (PDF, symbols). Note that the coarser resolution and lower sensitivity of the TMI retrievals shifts the low end of the TMI distributions towards larger values (for areas < 500 km^2).

As indicated by the area-weighted PDFs, the PR and TMI distributions are very similar overall (especially between 1 000 and 30 000 km^2), given the differences in resolution, light rain sensitivity, beamfilling (preferentially impacting the smaller end of the distribution), and swath width (impacting primarily the larger end of the distribution). Beyond the apparent truncation in the PR distribution at around 30 000 km^2, the TMI distribution maintains the same slope up until nearly 200 000 km^2. These results suggest that the PR swath width limit is not drastically biasing the precipitation feature size distribution below the mentioned apparent truncation point.

The PR over-ocean distribution has more rain area portioned to smaller features and large features than over land. The TMI shows a different pattern: over land (ocean) a higher relative portion of the total raining area is assigned to smaller (larger) features, with a crossover around 100 000 km^2. The TMI results are consistent with previous work using IR data (Machado and Rossow 1993).

The CDFs show that TMI features are generally larger in area than PR features, again consistent with the swath width differences and differences in pixel sizes. However, the relative area difference between land and ocean regions is switched between TMI and PR features. The PR (TMI) finds that continental (oceanic) features are larger. To examine this result further, Fig. 5 shows the fraction of PR-swath defined features containing no

TMI rainfall as a function of area over ocean (black line) and land (grey line) areas. It shows that a higher fraction of over-land PFs have no TMI rainfall than over ocean at a given area, especially below 10^3 km^2. This shows that in addition to the beamfilling effects seen over ocean, the resolution, sensitivity and surface screening effects in the scattering microwave retrieval over land (McCollum and Ferraro 2003; Nesbitt et al. 2004) cause a large fraction of small PR features to be missed. The fact that the PR retrievals use much more similar physics and resolution over both land and ocean relative to the TMI, it is presumed that the PR land-ocean differences in feature size estimates are more realistic.

To place the TRMM results within the context of previous works using different platforms and study areas, Fig. 6 shows the size distribution of various feature area and FMD results over land (a) and ocean (b), on a log-probability plot (distributions that form a straight line are log-normal). The size distribution of rainfall features has often been described as resembling a truncated lognormal distribution (López 1977; Williams and Houze 1987; Mapes and Houze 1993; Johnson et al. 1999). Previous distributions from Williams and Houze (1987, their Fig. 14) of IR cloud shield area < 213 K over land and ocean areas around the Maritime Continent are shown, along with results from Mapes and Houze (1993, their Fig. 3) using thresholds of 198 and 208 K over the broader West Pacific (plotted in b). Results from single ground-based radar studies of FMD are shown from Cruz et al. (1973) over northern Venezuela and Miller et al. (1975) from western North Dakota, multi-radar composite estimates of MCS FMD from Geerts (1998), and airborne radar-estimated FMD from López (1976) from an area of the Atlantic Ocean east of the Lesser Antilles.

While the distributions of IR feature areas in the studies shown here are taken over a limited area of the Tropics, they show a similar slope in the area distribution to the PR and TMI results, especially below the 95th percentile. Because the IR cold cloud area typically encompass non-raining cirrus anvils as well as precipitating convective and stratiform clouds, the IR distributions track well above the PR and TMI retrieved areas, except at the large end of the ocean distribution in (b), where TMI areas closely match the IR distributions. The reason why the TMI and IR size distributions become similar at the large end of the PF size spectrum is a topic for future research, but may be due to regional sampling differences between the two datasets.

FMD distributions derived from TRMM generally range to higher maximum values than those derived from single radars likely because the observation swath, while limited in the cross-track direction, is "unlimited" in the along track dimension. Ground based-radars typically only scan to 150-250 km, so unless multi-radar composites are generated (i.e. Geerts 1998), it is rare for large precipitation features (i.e. MCSs) to be scanned in their entirety.

PR and TMI feature and FMD distributions are much more similar over land (a) than ocean (b) for the resolution, sensitivity, and swath width differences discussed previously. These results suggest that the low frequency low-resolution channels of the TMI retrievals used over ocean likely bias feature size retrievals high, especially for small features. This reinforces that the land-ocean differences in the TMI algorithm make it difficult to perform objective regional comparisons, despite its wider swath. For this reason, the remainder of this study will focus on analysis with the PR, noting that the feature size distribution is truncated as shown above.

4. PF morphology and rainfall

Regional distributions of 3-year mean feature area and FMD determined from PR PFs are contoured (on a log scale) in Fig. 8 a and b respectively. In a broad sense, both measures show maxima at the climatological location of the ITCZ and in the Subtropics. Within the Tropics, the Sahel region in Africa stands out where features are largest by both measures. Moreover, the Congo basin has regions where features, on average, exceed 500 km^2; no regions within the Amazon basin or Maritime Continent exceed this value on average. Cross-Pacific variability includes larger features on each end of the ITCZ, with a minimum near 180° longitude. In the Subtropics, the semi-permanent highs near ±20° latitude lead to areas where oceanic PFs are small by both dimensional measures. However, with the exceptions of the Sahara and the Arabian Peninsula, all continental areas have features larger than their surrounding oceanic counterparts. Near ±35° latitude, feature sizes are generally larger than areas 10° equatorward, with maxima in both feature area and FMD over the La Plata Basin and the USA. Subtropical Oceanic maxima tend to occur (1) downstream of the continents where SSTs tend to be climatologically warmest, (2) in the storm tracks of extratropical cyclones and attendant frontal systems, and/or (3) within large-scale subtropical convergence zones (such as the South Atlantic or South Pacific Convergence Zones), all of which provide environments favorable for organized precipitation.

a) Rainfall and horizontal structure

Fig. 9 compares PDFs of the frequency of occurrence and rainfall fraction as a function of rain area and FMD over ocean and land areas. As shown in Fig. 5, ocean features are more numerous than land features at the small end of the area distribution

(Fig. 9a), while the reverse is true at the larger end of the distribution. The fractional rain volume contribution by feature area shows three regimes, whereby a mid range (bracketed by areas of 400 and 20 000 km^2) has higher relative contribution from features over land than over ocean; with the opposite true for small and large features on both sides of this range. The plot showing number and rainfall contributions by FMD show a similar distribution (Fig. 9b), with the three regimes of rain volume contribution as a function of FMD showing up in panel (b) as in (a) in terms of area.

b) Rainfall and vertical structure

To examine the effects of PF vertical structure on rainfall, Fig. 10 shows the number and rainfall fraction of features as a function of 4 proxies of PF maximum convective depth and/or intensity over ocean and land surfaces. Panel (a) and (b) show the above quantities as a function of maximum 17 and 30 dBZ ETH within each feature, respectively (note that features without 30 dBZ echo are plotted along the ordinate in b). In terms of number fraction, the distribution is shifted to higher heights for features over land relative to the ocean distribution, with a modal value at nearly 6 km (4.5 km) at 17 dBZ (30 dBZ) over land, while over ocean the modal value is near 2.5 km in both the 17 and 30 dBZ ETH. Several studies have shown that continental storms more often contain sufficiently robust vertical structures to produce lightning (Zipser and Lutz 1994; Nesbitt et al. 2000; Toracinta et al. 2000; Petersen and Rutledge 2001; Christian et al. 2003; Cecil et al. 2005).

When examining the rainfall distributions in context with the number distributions over land and ocean, note that the large number of shallow features with 17 dBZ ETHs below the freezing level do not contribute more than 15% of the rainfall over ocean or

more than 5% of the rainfall over land (Short and Nakamura 2000). The rainfall distributions are displaced in a land-ocean sense just as their number distributions, with a higher fraction of rainfall over land coming from deeper features (where mixed-phase processes are likely more involved in rainfall production). Note the trimodal distribution in rainfall by 17 dBZ echo top over ocean, with relative maxima in rainfall contributions from features with ETHs below the freezing level, at 8.5-10 km, and at roughly 15 km. Over land, the rainfall peak from below the freezing level is not nearly as evident as over ocean, however (perhaps due to different modal thermodynamic profiles or aerosol effects), more prominent peaks at 10-12 and 15-17 km are present in the land 17 dBZ ETH distributions. At 30 dBZ in (b), about 30% of oceanic and continental rainfall falls with echo tops between 5.5 and 6.5 km (which may be influenced by the enhancement of reflectivity by the bright band near 5 km in the Tropics); the ocean distribution (similar to that found in DeMott and Rutledge 1998) falls off more quickly than the land distribution, which has greater than 5% rainfall contributions from features up to nearly 13 km. The increased rainfall contribution from more vertically robust precipitation illustrates, in general, the increased significance of mixed phase processes to rainfall over land relative to ocean.

Panels (c) and (d) of Fig. 10 show the number and rainfall fraction from two other measures of convective vertical development, minimum VIRS IR T_b and minimum TMI 85 GHz PCT. Again, distinct differences exist among land and ocean locations, especially above 0°C in the IR distributions and 260 K in the 85 GHz distributions. Consistent with the ETH proxies described above, the large portion of features with warm T_bs in the IR and at 85 GHz do not produce significant rainfall contributions. The IR

number distribution over ocean has a peak warmer than 0°C which does cause a small rainfall peak, while over land the modal IR T_b is -10°C, corresponding with a small relative increase in rainfall contribution. Overall, the IR-land frequency histogram is shifted towards colder T_bs; and the rainfall distributions show a single rainfall peak at -70°C over land, while ocean rainfall contribution peaks, in addition to the one at previously mentioned at 15°C, occur at -50°C to -55°C and -70°C. Extremely cold IR T_bs (< -85°C) are likely related to overshooting convection penetrating the Tropical Tropopause Layer (e.g., Liu and Zipser 2005). Distributions at 85 GHz are similar between land and ocean regions in general, however higher fractional number and rainfall contributions occur at lower 85 GHz PCTs over land. Thus relatively higher optical depths of ice are responsible for rainfall processes over land, especially below 260 K (which is reflected in lightning-rainfall differences previously discussed).

5. Rainfall budgets

a) Rainfall contribution by feature type

In order to examine variability in regional rainfall characteristics, features are separated into four archetypical classes, each with characteristic diabatic heating profiles, based upon their PR horizontal and vertical structure. Table 1 lists the criteria of each of the feature types.

Shallow features are those that have no measurable PR reflectivity (>17 dBZ) at heights greater than 4.5 km MSL; it is recognized that there may be mixed or ice phase precipitation above this height not intense enough or not large enough in dimension to fill a PR resolution volume, or the freezing level may be somewhat lowered in the Subtropics. Precipitation from systems in this category, however, likely have a large

warm rain component (i.e. dominated by collision-coalescence mechanisms at temperatures > 0°C), and have latent heating confined to these shallow cloud depths. Small Cold features range from individual cumulus congestus clusters to organized deep convective clusters < 100 km in FMD and likely have a relatively small stratiform rain (and stratiform-mode latent heating) contribution, and mixed and ice phase precipitation growth occurring. Large Mid-level features are large in size, but do not meet the ETH criteria at 9.5 km. These features consist of weak or dissipating MCSs (and frontal systems in the Subtropics). They have a mix of convective and stratiform rain heating profiles, but are likely dominated by a stratiform rain and latent heating component due to the absence of deep convection according to the PR criteria selected here. The MCS definition used in this study aims to follow the Houze (1993) definition ("cloud systems that occur in connection with an ensemble of thunderstorms and produces a contiguous precipitation area ~ 100 km or more in at least one direction"), rather than the Nesbitt et al. (2000) 85 GHz ice scattering MCS definition[4] since radar FMD and ETH criteria are, in principle, less sensitive to convective intensity differences than 85 GHz ice scattering areal coverage and intensity criteria over land and ocean. Modal convective intensity differences (and storms' ability to loft precipitation-sized ice particles into the anvil) may unnecessarily affect the ice-scattering MCS classification.

MCSs have a deep convective and stratiform heating profile (Houze 1989), however relative contributions to total heating by MCSs vary by meteorological regime that lead to modal changes in convective intensity and convective-stratiform rain partitioning. The

[4] Nesbitt et al. (2000) defined an ice scattering MCS as a contiguous PR rain area containing at least 2000 km^2 of contiguous area with 85 GHz PCT $\leq$ 250 K, and containing at least 108 km^2 of non-contiguous areas with PCT $\leq$ 225 K. This definition was based on the 85-GHz only MCS definition of Mohr and Zipser (1996).

aim of this section is to quantify the relative and absolute contribution of these feature types to estimate how the superposition of these varying rainfall and latent heating regimes vary regionally.

To contrast bulk land-ocean differences in precipitation characteristics, and precipitation by system types, Table 2 shows feature populations, number fraction, mean conditional and unconditional rain rates[5], and horizontal size characteristics (mean area and FMD) over all ocean and land areas, while Table 3 examines population and feature size characteristics for the 4 feature types outlined above. Consistent with Short and Nakamura (2000), Shallow features dominate the population over ocean (Table 3); however this feature type occurs less frequently than Small Cold features over land. MCSs are slightly more (nearly twice as) numerous than Large Mid-Level features over ocean (land). Despite indications that oceanic features have less convective intensity (i.e., less robust vertical structure) than continental features, consistent with differences in bulk buoyancy profiles (Fig. 10, Nesbitt et al. 2000; Toracinta et al. 2001; Petersen and Rutledge 2001; Cecil et al. 2005), all categories of features are larger in terms of both mean area and FMD over ocean than over land.

The fraction of rainfall by the four feature types in annual-average 2.5° boxes (smoothed with a 1:10:1 box filter in both dimensions) is contoured in Fig. 11a-d. While feature populations are dominated by Shallow features as shown above, Fig. 11d shows that rainfall (and bulk latent heating) are dominated by the MCSs in most heavily raining

[5] The unconditional rain rate (RR_{uncond}) is calculated as the mean rain rate over all raining and nonraining pixels, while the conditional rain rate (RR_{cond}) is the mean rain rate over raining pixels only. Furthermore, total unconditional rain rate can be broken down by feature type since this quantity may be thought of as the sum of the unconditional rain rates over all feature types.

areas of the Tropics and Subtropics. The La Plata Basin sees MCS rainfall contributions nearing 90 percent of total rainfall; the Sahel, Congo Basin, south central US (consistent with Fritsch et al. 1986), and the west coast of Central America/nearby East Pacific see MCS contributions exceeding 70 percent. Most other heavily raining Tropical areas have MCS rainfall contributions of at least 50 percent over both land and ocean. Note the interesting cross-Pacific variability, however. MCS contributions gradually fall off from high fractions in the extreme East Pacific to values near 50 percent in the Central Pacific. MCS rainfall is replaced by increased fractions in Shallow, Small Cold, and Large Mid-Level features near the dateline. This indicates that features are less vertically intense and horizontally developed in the central Pacific relative to the East. In the West Pacific, MCS and Small Cold fractions increase above 70 and 20 percent, respectively. Large Mid-Level and Shallow fractions decrease in compensation to the increasing MCS and Small Cold contributions westward towards the Maritime Continent. This Cross-Pacific variability in PF type has important ramifications for the water cycle over the Pacific and large-scale circulation in the region (Schumacher et al. 2004).

Fig. 11e shows the fraction of rainfall from features exceeding 100 km in FMD (the sum of MCS and Large Mid-Level features), while Fig. 11f shows the fraction of rainfall from 85 GHz ice scattering MCSs according to the Nesbitt et al. (2000) definition. Comparison of panels d through f reveal the sensitivity of the estimated rainfall contribution based on a radar definition using horizontal and vertical structure information (panel d), horizontal structure only (panel e), and a ice scattering definition which takes into account horizontal and vertical structure information (panel f). The ice scattering MCS definition (in f) is met comparatively more often in regions where

convective intensity and areal coverage is stronger relative to ocean areas (e.g., Schumacher et al. 2003a; Cecil et al. 2005), while the radar definition of an MCS (in d) equalizes rainfall contribution among these regions more than the ice scattering definition. Considering solely horizontal structure information in the feature definition (in e) in the Tropics and Subtropics, the combination of Large-Mid Level features with the radar-defined MCSs (or all features with FMD > 100 km except Shallow features) makes the rainfall contributions the most equivalent within the domain studied here among these PF criteria, although the modal environmental forcings, precipitation vertical structures, and microphysical mechanisms differ between these regions (and as a function of season, especially in the case of the Subtropics).

With the goal of examining how these archetypical cloud system types contribute to total rainfall regionally (with implications for cloud ensemble parameterization), Fig. 12 shows the unconditional rain rate (in mm/day) from each of the four feature types described above as a function of total unconditional rain rate. In other words, each point represents each feature type's contribution to unconditional rain rate as a function of the total rain rate in each 2.5° x 2.5° grid box shown in Fig. 11, separated between points over ocean (a) and land (b). Over ocean (a) at low rain rates (< 1 mm dy^{-1}), Shallow features dominate the contribution to total rainfall, while over land the rain producers at these low rain rates are largely Small Cold features and MCSs. Fig. 11 shows that areas dominated by Small Cold features at these low unconditional rain rates mainly exist over the oceanic subtropical highs and continental mountainous areas and deserts. There are also areas where Large Mid-Level features produce around 50 percent of the total ocean rainfall at an unconditional rain rate around 1 mm dy^{-1} (Fig. 12a); these are areas where

frontal precipitation likely plays an important role in rainfall production in the Subtropics (Fig. 11). At higher unconditional rain rates (in the 1-3 mm dy^{-1} range) over ocean (Fig. 12a), both MCSs and Small Cold features continue to increase in fractional rainfall contribution. While the same is true for MCSs over land in this unconditional rain rate range, Small Cold features begin to cluster around 30 to 40 percent rainfall conribution.

Above 3 mm dy^{-1} over both land and ocean, the separation of feature types becomes much more clear (and constant) in terms of fractional rainfall contribution. In this rain rate range, MCSs dominate the rainfall budget over both land and ocean (contributing at least half the rain volume in most areas), with land areas having higher extreme values (in selected subtropical areas with > 80 percent MCS rain contribution, c.f. Fig. 11). Small Cold rainfall fractions settle out to near a value of 0.25 to 0.30, higher (lower) than values at lower rain rates over ocean (land). Large Mid-Level and Shallow features contribute less than 20 and 10 percent of total rainfall over ocean and land, respectively, for most unconditional rain rates > 3 mm dy^{-1}.

Fig. 12 shows that there are clear relationships between cloud system populations and total rain rate, and the environments associated with these archetypical cloud system types likely provide limitations on rainfall production. Shallow features rarely contribute more than 1 mm dy^{-1} over ocean, and 0.4 mm dy^{-1} over land, even in areas with high total rain rates[6]. Large Mid-Level features maximize their contribution when the total rain rate is near 3 mm dy^{-1}; however, these features contribute less than 1.1 mm dy^{-1} and, as shown in Fig. 11, while Large Mid-Level features tend to occur in the Subtropics. Over both land and ocean, it is the presence of MCSs, and to a lesser extent Small Cold

[6] This is the case at least in 2.5° grid resolution data. Shallow orographic precipitation is known to produce a high localized rainfall rate, for example.

features, that allow the total rain rate to exceed about 1-2 mm dy^{-1} in most regions, and it is almost exclusively MCSs that allow the total rain rate to exceed 2.5 mm dy^{-1}. These results suggest it may be plausible to parameterize variability in Tropical cloud ensemble populations based upon underlying surface and total rain rate. Such parameterizations would be useful as a constraint in rain rate and latent heating distributions.

b) Diagnosing rainfall budgets

Table 4 shows selected characteristics of the classified feature populations relevant to rainfall budget considerations. The distribution of rainfall fraction by feature type (identical to that shown in Fig. 11) shows distinct differences over land and ocean. Shallow features contribute 12% of the rainfall over ocean and only 2% over land. Small Cold features are responsible for nearly 1/3 of the rainfall over land, while only 1/5 of the rainfall over ocean. Thus, small deep (shallow) features with accompanying mixed phase (warm rain) processes contribute more rainfall over land (ocean), which may be related to underlying buoyancy differences (Lucas et al. 2000). Oceanic Large Mid-Level features are responsible for nearly twice the rainfall contribution over ocean as over land. MCSs contribute three-fifths of the total rainfall over land and just over half the rain over the ocean. However, when considered together, MCS and Large Mid-Level features contribute equal fractions (0.69) of total rainfall, despite the vertical structure differences implied in the definition.

To quantitatively diagnose how feature types contribute to the total regional rainfall, a framework is defined based upon observable quantities related to PF morphology and rainfall intensity. Here, the total conditional rain rate, as well as convective and stratiform conditional rain rates can be calculated by considering the total and so-

classified portions of rainfall separately. Conditional rain rates are highest in MCS features (Table 4), followed by Small Cold, Large Mid-Level, and Shallow features. MCS features have the highest conditional, convective, and stratiform rain rates due to many factors including their required deep structure (cold microphysical processes play a large role in precipitation generation), their mesoscale dynamics enhancing precipitation intensity, as well as their physical size minimizing beamfilling effects. Despite the MCS stratiform fraction being higher over ocean (which lowers total conditional rain rate because the stratiform conditional rain rate is less than the convective conditional rain rate), the MCS rain volume per feature is higher over ocean than land due to MCS conditional rain rates and mean areas being larger over ocean (Table 3) than over land.

Small Cold features are second in terms of mean conditional rain rate, but have lower convective and stratiform conditional rain rate values than Large Mid-Level features. However, Large Mid-Level features have lower total conditional rain rates than Small Cold features because they have higher stratiform area fractions (and thus higher stratiform rain fractions). Shallow features have the lowest conditional rain rate because (1) they rely more on warm rain processes for droplet growth over more efficient mixed-phase processes, and (2) partial beamfilling tends to lower conditional rain rates preferentially in this feature type due to their small size.

To examine the regional variability in rain budgets, Fig. 13a shows a contour map of rain volume per feature, which clearly shows that the mean rain volume per feature is higher over most land areas relative ocean areas when all features are taken into account. This is the case because the land rain budget contains a higher relative fraction of rain features that have relatively higher conditional rain rates. MCSs and Small Cold features

(which have higher conditional rain rates than Large Mid-Level and Shallow features, Table 4) constitute a three times higher fraction of the population (and 7% and 9% higher rainfall fraction, respectively) over land than ocean. The oceanic rain budget contains a 12% rainfall contribution from Shallow features (compared to 2% over land), with a conditional rain rate of 1.9 mm/hr. This serves to lower the ocean rain volume per feature (and mean unconditional rain rate in Table 2) relative to land. Large Mid-Level features, in bulk, do not serve to modify the land and ocean conditional rain rate significantly since their feature conditional rain rate is similar to the total conditional rain rate. Beyond the bulk land/ocean differences presented here, many important regional differences exist, such as the good correspondence between increased rain volume per feature and MCS fractional rainfall contribution shown in Fig. 12, especially in areas like the Sahel, Congo, La Plata Basin, and SE USA. Despite heavy rainfall in the central Pacific Ocean (> 3 mm dy^{-1}), the mean rain volume per feature is low compared with most areas experiencing similar or greater average annual rainfall.

Similar reasoning as above accounts for the fact that mean conditional rain rates are slightly higher over land areas than ocean areas (Table 2, Fig. 13b). Since each of the features are raining more on average and the mean conditional rain rate is higher over land areas, this has implications on the frequency of occurrence of precipitating features. From the above equations, it is possible to estimate the number of PFs TRMM would sample if it were measuring the global Tropics and sub-Tropics constantly, since we can estimate the unconditional rain rate, and thus the total rain volume observed. Consider the ratios of rain volume observed and the actual rain rate:

$$\frac{\left(\sum R_{\text{vol}}\right)_{obs}}{\left(\sum R_{\text{vol}}\right)_{tot}} = \frac{\left(n_f \overline{A}\,\overline{RR_{\text{cond}}}\right)_{obs}}{\left(n_f \overline{A}\,\overline{RR_{\text{cond}}}\right)_{tot}}, \tag{2}$$

where $\sum R_{vol}$ is the total volumetric rain, n_f is the number of PFs, $\overline{A}$ is the mean PF area, and $\overline{RR_{\text{cond}}}$ is the mean conditional rain rate of PFs under consideration. The subscripts *obs* and *tot* indicate the TRMM-observed quantities and the values that would be observed if TRMM were sampling continuously, respectively. Assuming that mean conditional rain rates and areas are constant (keeping in mind that TRMM PR areas tend to bias the true raining areas of small and large features), and noting that $\left(\sum R_{vol}\right)_{tot} = A_{box} RR_{\text{uncond}}$ (where A_{box} and RR_{uncond} are the areas and unconditional rain rate in an area of interest) it can be shown that:

$$\left(n_f\right)_{tot} = \left(n_f\right)_{obs} \frac{RR_{\text{uncond}} A_{box}}{\left(\sum R_{\text{vol}}\right)_{obs}}, \tag{3}$$

where $\left(n_f\right)_{obs}$ is the number of features observed by TRMM and $\left(n_f\right)_{tot}$ is the estimated number of features observed by TRMM if it were observing continuously. Fig. 13c shows a contour map of $\left(n_f\right)_{tot}$ (on a log scale per 2.5° grid box per year) estimated from this technique. These results shows order-of-magnitude differences in this quantity between Sub-Saharan Africa and the Northern Amazon, where fewer, more intensely raining features in sub-Saharan Africa (as evidenced by panels b and c) contribute to similar rainfall amounts (as shown by the unconditional rain rate contours) as observed over in the northern Amazon basin. Subtropical land regions see especially large rain volumes per feature (Fig. 13a) and conditional rain rates (Fig. 13b), but smaller numbers of features (Fig. 13c) reduce total rain rates. Over the oceans, a similar number of

features in subtropical relative to tropical regions (or even significantly more features over the northwest and South Pacific Convergence Zone relative to the Pacific ITCZ) rain less (in terms of volume and intensity) per feature, leading to significantly less total rainfall within the Subtropical high belt.

6. Summary

The morphology and rainfall characteristics of PFs based on three years of data from the TRMM satellite's Precipitation Radar is analyzed in context with previous studies examining the size distribution of features (from IR and ground- and aircraft-based radars), and those from the TRMM Microwave Imager (whose swath is more than 3 times as wide as the PR's). Total rain area and FMD (determined by an objective ellipse-fitting technique) are used to quantify the horizontal extent of features. Comparisons of PR and TMI rain areas show that number-area fractions are very similar in the 1 000 to 30 000 km^2 range, both in slope and in the fact that land areas tend to have more features in this size range than at smaller or larger sizes. However, at small sizes, the TMI retrievals bias the feature distribution relative to the PR; this is attributed to differences in pixel resolution over land and ocean with the TMI. This, along with the fact that the PR has higher precipitation sensitivity and higher resolution, makes the PR a more objective quantifier of feature size at small values in terms of quantifying land-ocean differences. At large feature sizes, the TMI is able to properly resolve features due to its wider swath. At MCS size criteria (FMD > 100 km), the PR is able to fully resolve nearly 80 percent of such features, which is considered sufficient to estimate their regional rainfall contribution, especially in the Tropics where features are smaller than subtropical frontal features.

Comparisons of feature area and FMD with previous studies using IR and scanning radar platforms show that the TRMM-derived estimates are physically consistent given the different areas of observation and data characteristics. The TMI and PR have higher resolution and a more physically direct relation to precipitation and latent heating than previous IR studies, and thus they are able to account for smaller features in regional comparisons of feature size. Interestingly, the slope of the PR and TMI size distributions of area and FMD are very similar and both approach the maximum IR size distributions derived over the West Pacific by Mapes and Houze (1993). While different areas are sampled (West Pacific versus entire TRMM domain), this finding needs further investigation and may indicate that feature size information may improve IR-rainfall estimation techniques. PR and TMI area and FMD distributions are much more representative of natural variability of feature sizes at the large end of the spectrum compared with single ground- and aircraft-based radars because of their virtually unlimited swath in the along-track direction. Given the 20 dBZ reflectivity threshold for defining features in this study, future work (using more sensitive radars such as CloudSat or the more sensitive precipitation radar planned for the Global Precipitation Mission core satellite) will aim to quantify the impact of higher sensitivity to feature size estimates.

Feature sizes are shown to have large sub-regional variability not necessarily correlated with local rainfall intensity, leading to apparent discrepancies in regional comparisons of rainfall characteristics. The population of (rainfall from) oceanic rainfall systems is dominated more by features of small (small and large) horizontal extent compared with those over land, while features having mid-sized horizontal extent tend to

be more important over land in terms of number and rainfall. Measures of peak convective intensity show that vertical structure-rainfall relationships also differ significantly over land and ocean. Generally speaking, rainfall over land is produced by systems that are *considerably more vertically developed* compared with oceanic rainfall systems, whether it is categorized by radar, passive microwave, or IR convective intensity measures. These land-ocean differences in vertical and horizontal structure within rainfall systems infer characteristic differences in the microphysical modes leading to rainfall production in these regions, and has implications in terms of regional radiative and latent heating distributions from precipitation systems.

Features have been separated into four categories by their vertical and horizontal structure characteristics to elucidate regional differences in rainfall budgets; these characteristics were selected based on their archetypical microphysical rainfall and latent heating vertical structure and horizontal extent produced by these systems. MCSs are shown to be the dominant rainfall producer in most heavily raining areas of the Tropics and Subtropics (contributing 50 to 90 percent of the total rainfall); rainfall contributions by MCSs (and to a lesser extent, Small Cold features) allow local unconditional rain rates to exceed 1.0 mm dy^{-1} (at 2.5° resolution). Strong regional gradients in MCS rain fraction exist (even as unconditional rain rate is conserved). However, when the Nesbitt et al. (2000) ice scattering definition is compared with this study's radar-only definition of an MCS (modeled after Houze 1993) the regional gradients in MCS rainfall fraction are increased (due to the former definition's insistence on more robust convective processes occurring within the system, which occur preferentially over land).

While MCSs dominate rainfall production (in terms of both fraction and amount) in many regions examined herein, this study finds many regions where MCSs are not as important in terms of rainfall fraction. First, some regions contain local increased fraction of less intense, but horizontally extensive features (Large Mid-Level features) that are either extremely weak or dissipating MCSs, or frontal systems in the Subtropics. In either case stratiform fractions are high in these regions (Schumacher and Houze 2003a), indicating a relative lack of intense convection due to a lack of moist-convective instability or sufficient shear in order to maintain long-lived convective systems (e.g., Weismann and Klemp 1984). Secondly, increased relative contributions from Small Cold features over mountainous and dry land regions indicate areas where features less often grow horizontally upscale to MCSs (where environmental moisture or shear is insufficient to maintain MCSs). Thirdly, increased fractions of rainfall from shallow systems over oceanic regions indicate the possible location of more intense trade-wind inversions, as in the upwelling regions of the Tropical oceans relative to the rest of that ocean's ITCZ.

The combination of regional variations in the amount of precipitation per rainfall system, and the frequency of occurrence and the areal coverage of those precipitation systems leads to widely varying precipitation regimes within the Tropics, with rainfall coming from more features with less rainfall volume on average over ocean than land. However, when examining the rainfall by feature size distributions in detail, small and large (mid-sized) features are responsible for a higher fraction of rainfall over ocean (land). These regional differences in rain budgets by feature type strongly impact regional climate, water cycles, and the diabatic response from convective systems. Since

the global circulation is sensitive to regional gradients in latent heating distributions (Hartmann et al. 1984, Schumacher et al. 2004), it is hypothesized that climate simulations must be able to simulate variability in cloud systems in order to represent global, and particularly regional climate change. These results show that there is characteristic variability in cloud ensemble populations as a function of total rainfall rate and underlying surface type, which may provide insight in developing, and an important constraint upon, new types of convective parameterizations. Evaluating the ability of cloud resolving models to reproduce the TRMM-derived regional variability of cloud systems will be a goal of future work.

Acknowledgements

This research was supported by NASA Precipitation Measurement Mission funding (grant NAG5-13623) under the direction of Dr. Ramesh Kakar. Thanks go to Dr. Daniel Cecil, Dr. Chuntao Liu, Prof. Edward Zipser, Prof. Robert A. Houze, Jr., and Dr. Timothy Lang for helpful science discussions, as well as Paul Hein, Margi Cech, and Jillian L'Ecuyer for administrative support. The three reviewers also provided careful and insightful comments that were much appreciated. Special thanks go to Drs. Erich Stocker and John Kwiatkowski and the rest of the TRMM Science Data and Information System (TDSIS) at NASA Goddard Space Flight Center, Greenbelt, MD, for data processing assistance.

References

Biondini, R., 1976: Cloud motion and rainfall statistics. *J. Appl. Meteor.,* **15,** 205–224.

Cecil, D. J., S. J. Goodman, D. J. Boccippio, E. J. Zipser, and S. W. Nesbitt, 2005: Three years of TRMM precipitation features. Part I: Radar, radiometric, and lightning characteristics. *Mon. Wea. Rev.*, **133**, 543-566.

Cetrone, J., and R. A. Houze, Jr., 2006: Characteristics of tropical convection over the ocean near Kwajalein. *Mon. Wea. Rev.*, in press.

Christian, H. J., and Coauthors, 2003: Global frequency and distribution of lightning as observed from space by the Optical Transient Detector. *J. Geophys. Res.*, **108**, 4005, doi:10.1029/2002JD002347.

DeMott, C. A., and Rutledge S. A., 1998: The vertical structure of TOGA COARE convection. Part I: Radar echo distributions. *J. Atmos. Sci.,* **55**, 2730–2747.

Fritsch, J. M., R. J. Kane, and C. R. Chelius, 1986: The contribution of mesoscale convective weather systems to the warm-season precipitation in the United States. *J. Climate Appl. Meteor.,* **25,** 1333–1345.

Geerts, B., 1998: Mesoscale convective systems in the southeast United States during 1994-95: A survey. *Wea. Forecasting*, **13**, 860-868.

Hartmann, D. L., H. H. Hendon, and R. A. Houze Jr., 1984: Some implications of the mesoscale circulations in tropical cloud clusters for large-scale dynamics and climate. *J. Atmos. Sci.,* **41,** 113–121.

Hitchfeld, W. F., and J. Bordan, 1954: Errors inherent in the radar measurement of rainfall at attenuating wavelengths. *J. Meteor.*, **11**, 58–67.

Houze, Jr., R. A., 1989: Observed structure of mesoscale convective systems and implications for large-scale heating. *Quart. J. Roy. Meteor. Soc.,* **115,** 425–461.

——, and C. Cheng, 1977: Radar characteristics of tropical convection observed during GATE: Mean properties and trends over the summer season. *Mon. Wea. Rev.,* **105,** 964–980.

——, and A. K. Betts, 1981: Convection in GATE. *Rev. Geophys. Space Phys.,* **19,** 541–576.

——, 1993: *Cloud Dynamics.* Academic Press, 573 pp.

Iguchi, T., and R. Meneghini, 1994: Intercomparison of single-frequency methods for retrieving a vertical rain profile from airborne or spaceborne radar data. *J. Atmos. Oceanic Technol.,* **11**, 1507–1517.

——, T. Kozu, R. Meneghini, J. Awaka, and K. Okamoto, 2000: Rain-profiling algorithm for the TRMM precipitation radar. *J. Appl. Meteor.,* **39**, 2038–2052.

Johnson, R. H., Rickenbach T. M., Rutledge S. A., Ciesielski P. E., and Schubert W. H., 1999: Trimodal characteristics of tropical convection. *J. Climate.,* **12**, 2397–2418.

Keenan, T. D., and Carbone R. E., 1992: A preliminary morphology of precipitation systems in tropical northern Australia. *Quart. J. Roy. Meteor. Soc.*, **118**, 283–326.

Kummerow, C. D., W. Barnes, T. Kozu, J. Shiue, and J. Simpson, 1998: The Tropical Rainfall Measuring Mission (TRMM) sensor package. *J. Atmos. Oceanic Technol.,* **15,** 809–817.

——, and coauthors, 2000: The status of the Tropical Rainfall Measuring Mission (TRMM) after two years in orbit. *J. Appl. Meteor.*, **39**, 1965-1982.

——, and coauthors, 2001: The evolution of the Goddard profiling algorithm (GPROF) for rainfall estimation from passive microwave sensors. *J. Appl. Meteor.,* **40**, 1801–1820.

Liu, C., and E. Zipser: 2005: Global distribution of convection penetrating the tropical tropopause. *J. Geophys. Res.*, **110** (D23), 104, doi:10.1029/ 2005JD006063.

López, R. E., 1976: Radar characteristics of the cloud populations of tropical disturbances in the northwest Atlantic. *Mon. Wea. Rev.,* **104,** 268–283.

——, 1977: The lognormal distribution and cumulus cloud populations. *Mon. Wea. Rev.,* **105,** 865–872.

——, 1978: Internal structure and development processes of C-scale aggregates of cumulus clouds. *Mon. Wea. Rev.,* **106,** 1488–1494.

Lucas, C., Zipser E. J., and Ferrier B. S., 2000: Sensitivity of tropical West Pacific oceanic squall lines to tropospheric wind and moisture profiles. *J. Atmos. Sci.*, **57**, 2351–2373.

Machado, L. A. T., and Rossow W. B., 1993: Structural characteristics and radiative properties of tropical cloud clusters. *Mon. Wea. Rev.,* **121**, 3234–3260.

Mapes, B. E., and Houze R. A., 1993: Cloud clusters and superclusters over the oceanic warm pool. *Mon. Wea. Rev.,* **121**, 1398–1415.

Medioni, G., M.-S. Lee, and C. K. Tang, 2000: *A computational framework for segmentation and grouping*. Elsevier Publishing, 260 pp.

McCollum, J. R., and R. R. Ferraro, 2003: The next generation of NOAA/NESDIS TMI, SSM/I, and AMSR-E microwave land rainfall algorithms. *J. Geophys. Res.*, **108**, 8382, doi:10.1029/ 2001JD001512.

Miller, J. R., A. S. Dennis, J. H. Hirsch, and D. E. Cain, 1975: Statistics of shower echoes in western North Dakota. Preprints, *16th Radar Meteorology Conf.,* Houston, TX, Amer. Meteor. Soc., 391–396.

Mohr, K. I., and E. J. Zipser, 1996: Mesoscale convective systems defined by their 85 GHz ice scattering signature: Size and intensity comparison over tropical oceans and continents. *Mon. Wea. Rev.*, **124**, 2417-2437.

Nesbitt, S. W., E. J. Zipser, and D. J. Cecil, 2000: A census of precipitation features in the Tropics using TRMM: Radar, ice scattering, and lightning observations. *J. Climate*, **13**, 4087-4106.

——,, and ——,, 2003: The diurnal cycle of rainfall and convective intensity according to three years of TRMM measurements. *J. Climate.,* **16**, 1456–1475.

——,, ——,, and C. D. Kummerow, 2004: An examination of version 5 rainfall estimates from the TRMM microwave imager, precipitation radar, and rain gauges on global, regional and storm scales. *J. Appl. Meteor.*, **43**, 1016-1036.

Petersen, W. A, and S. A. Rutledge, 2001: Regional variability in tropical convection: Observations from TRMM. *J. Climate*, **14**, 3566–3586.

Rickenbach, T. M., and S. A. Rutledge, 1998: Convection in TOGA COARE: Horizontal scale, morphology, and rainfall production. *J. Atmos. Sci.*, **55**, 2715-2729.

Rickenbach, T. M., 1999: Cloud-top evolution of tropical oceanic squall lines from radar reflectivity and infrared satellite data. *Mon. Wea. Rev.,* **127**, 2951–2976.

Schumacher, C., and R. A. Houze, Jr., 2003a: Stratiform rain in the Tropics as seen by the TRMM precipitation radar. *J. Climate*, **16**, 1739-1756.

——, ——, 2003b: The TRMM Precipitation Radar's view of shallow, isolated rain. *J. Appl. Meteor.,* **42**, 1519–1524.

——, ——, and I. Kraucunas, 2003: The Tropical dynamical response to latent heating estimates derived from the TRMM precipitation radar. *J. Atmos. Sci.*, accepted.

Simpson, J., R. F. Adler, and G. R. North, 1988: A proposed Tropical Rainfall Measuring Mission (TRMM) Satellite. *Bull. Amer. Meteor. Soc.*, **69**, 278-295.

Short, D. A., and K. Nakamura, 2000: TRMM radar observations of shallow precipitation over the tropical oceans. *J. Climate*, **23**, 4107-4124.

Spencer, R. W., H. M. Goodman, and R. E. Hood, 1989: Precipitation retrieval over land and ocean with the SSM/I: Identification and characteristics of the scattering signal. *J. Atmos. Oceanic Technol.,* **6,** 254–273.

Takayabu, Y. N., 2002: Spectral representation of rain profiles and diurnal variations observed with TRMM PR over the equatorial area, *Geophys. Res. Lett.*, **29**, doi:10.1029/2001GL014113.

Toracinta, E. R., D. J. Cecil, E. J. Zipser, and S. W. Nesbitt, 2002: Radar, passive microwave, and lightning characteristics of precipitating systems in the Tropics. *Mon. Wea. Rev.,* **130**, 802-824.

Weisman, M. L., and J. B. Klemp, 1984: The structure and classification of numerically simulated convective storms in directionally varying wind shears. *Mon. Wea. Rev.,* **112,** 2479–2498.

Williams, M., and R. A. Houze, Jr., 1987: Satellite-observed characteristics of winter monsoon cloud clusters. *Mon. Wea. Rev.,* **115,** 505–519.

Zipser, E. J., and Lutz K. R., 1994: The vertical profile of radar reflectivity of convective cells: A strong indicator of storm intensity and lightning probability?. *Mon. Wea. Rev.*, **122**, 1751–1759.

Table Captions

Table 1. FMD and ETH criteria for the four feature types examined in this study.

Table 2. Feature populations and characteristics over ocean and land.

Table 3. Populations and horizontal extent characteristics over land and ocean for the four feature types.

Table 4. Rainfall characteristics over land and ocean for the four feature types.

Figure Captions

Fig. 1. Schematic of two scenes containing PFs within the PR swath. In (a) and (c), VIRS 10.7 μm T_b (shaded within the PR swath) and 85 GHz PCT (contoured within and outside the PR swath). In (b) and (d) for the same scene, PR near surface reflectivity (contoured), LIS lightning flashes (+ signs), and locations of best fit ellipses of PFs within each scene. Within the largest feature in each scene, the major and minor axes of the best fit ellipse are labeled.

Fig. 2. Shaded log-log density plot of feature rain area versus ellipse fit area.

Fig. 3. CDFs of (a) feature area and (b) FMD for all features (dark solid lines), non-edge features (grey solid lines), and edge features (dashed grey lines).

Fig. 4. Contour maps of: (a) the number fraction of edge features (b) the rainfall fraction of edge features.

Fig. 5. Fraction of features within each area bin (dots) and CDFs of feature area (lines) for the TMI PFs (filled dots, thin lines) and PR PFs (open circles, thick lines) over ocean (black lines and symbols) and land (grey lines and symbols). The bins range from 1 to 7.3 by 0.3 in log area space.

Fig. 6. Fraction of features within each area bin with no TMI rainfall. Bins range from 1.25 to 7 log km^2 by 0.04 log km^2.

Fig. 7. On a log-probability plot: PR PF (open circles) and TMI PF (filled circles) rain area (black symbols) and FMD (grey symbols) over land (a) and ocean (b). Selected previous studies of IR cloud shield area and radar FMD are overlain. See the text for more details.

Fig. 8. (a) Log-contour map of mean feature rain area (km^2), (b) contour map of mean feature maximum dimension (km).

Fig. 9. Number fraction (dashed lines) and rain volume fraction (solid lines) of features over ocean (dark lines) and land (grey lines) as a function of (a) rain area (km^2) and (b) FMD (km). The bins in area range from 1.5 to 5.25 by 0.25 in log km^2 space, while in FMD they range from 0.6 to 3.6 by 0.3 in log km space.

Fig. 10. Number fraction (dashed lines) and rain volume fraction (solid lines) of features over ocean (dark lines) and land (grey lines) as a function of (a) PR maximum 17 dBZ ETH (km), (b) PR maximum 30 dBZ ETH (km), (c) VIRS minimum IR T_b (°C), and (d) TMI minimum 85 GHZ PCT (K). The bins for panels a and b range from 0 to 20 km by 1 km, while for panel c (d) they range from -95 to 15°C by 5°C (45 to 300 K by 5 K).

Fig. 11. Shaded contour map of fraction of rainfall by feature type. See text for details.

Fig. 12. Scatter diagrams of feature unconditional rain rate (mm dy^{-1}) (see legend at bottom) versus total unconditional rain rate (mm dy^{-1}) in 2.5° grid boxes over ocean (a) and land (b). Fraction of rain contours appear on the diagram as diagonal lines and are labeled at right.

Fig. 13. Shaded contour maps of (a) log mean rain volume per feature (mm hr^{-1} km^2), (b) mean conditional rain rate (mm hr^{-1}), and (c) log estimated number of features per year in each 2.5° box. The 1, 3, and 6 mm dy^{-1} contours of PR unconditional rain rate are shown by the white solid, long, and short dashed lines, respectively.

Table 1. FMD and ETH criteria for the four feature types examined in this study.

PF Type	FMD criteria	ETH criteria
Shallow	-	ETH ≤ 4.5 km (MSL)
Small Cold	FMD < 100 km	ETH > 4.5 km
Large Mid-level	FMD ≥ 100 km	4.5 > ETH > 9.5 km
MCS	FMD ≥ 100 km	ETH ≥ 9.5 km

Table 2. Feature populations and characteristics over ocean and land.

	Ocean	Land
Number of features ($\times 10^3$)	15389	2733
Number fraction	.82	.18
Mean conditional rain rate (mm hr^{-1})	2.71	2.81
Mean unconditional rain rate (mm dy^{-1})	2.48	2.02
Mean feature area (km^2)	189	371
Mean FMD (km)	17	21
Fraction of rain stratiform	.54	.48

Table 3. Populations and horizontal extent characteristics over land and ocean for the four feature types.

	Shallow		Small Cold		Large Mid-Level		MCS	
	Ocean	Land	Ocean	Land	Ocean	Land	Ocean	Land
Number of features ($\times 10^3$)	12108	1067	3101	1600	82	21	98	45
Number fraction	.787	.391	.202	.585	.005	.008	.006	.016
Mean feature area (km^2)	50	42	205	170	6358	5605	11166	9445
Mean FMD (km)	12	10	26	21	175	170	215	205

Table 4. Rainfall characteristics over land and ocean for the four feature types.

	Shallow		Small Cold		Large Mid-Level		MCS	
	Ocean	Land	Ocean	Land	Ocean	Land	Ocean	Land
Fraction of rainfall	.12	.02	.20	.29	.16	.09	.53	.60
Mean conditional rain rate (mm/hr)	1.90	1.66	3.07	3.36	2.95	2.48	4.74	4.52
Mean convective conditional rain rate (mm/hr)	2.5	2.7	7.0	7.8	9.4	9.1	12.8	11.5
Mean stratiform conditional rain rate (mm/hr)	1.3	1.2	1.7	1.6	2.2	2.0	3.2	2.8
Stratiform area fraction	.51	.69	.73	71	.90	.92	.84	.80
Stratiform rain fraction	.35	.49	.40	.34	.69	.74	.56	.50
Mean rain volume per feature (mm hr^{-1} km^2)	95	70	627	572	18759	13916	52970	42680

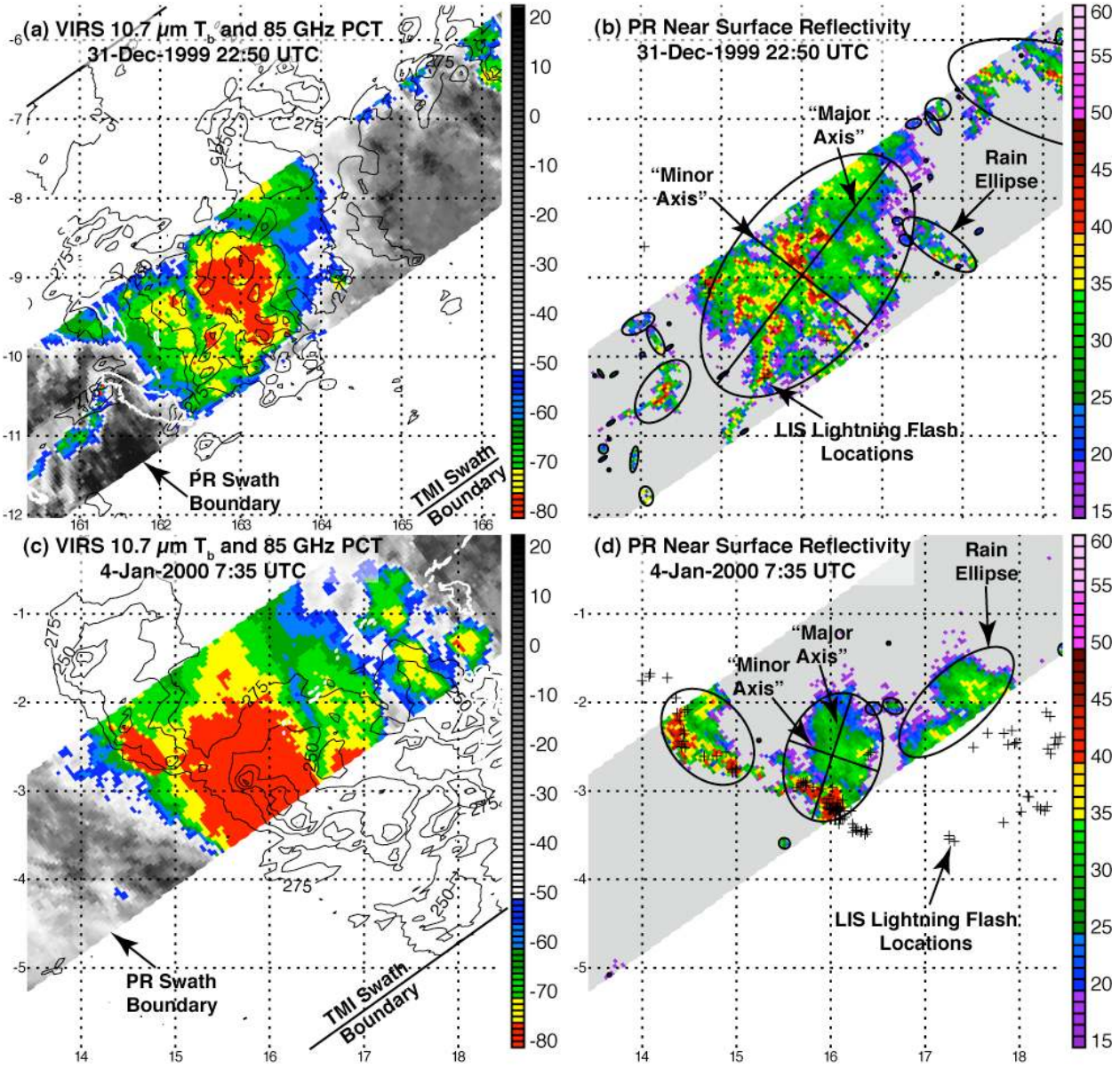

Fig. 1. Schematic of two scenes containing PFs within the PR swath. In (a) and (c), VIRS 10.7 μm T_b (shaded within the PR swath) and 85 GHz PCT (contoured within and outside the PR swath). In (b) and (d) for the same scene, PR near surface reflectivity (contoured), LIS lightning flashes (+ signs), and locations of best fit ellipses of PFs within each scene. Within the largest feature in each scene, the major and minor axes of the best fit ellipse are labeled.

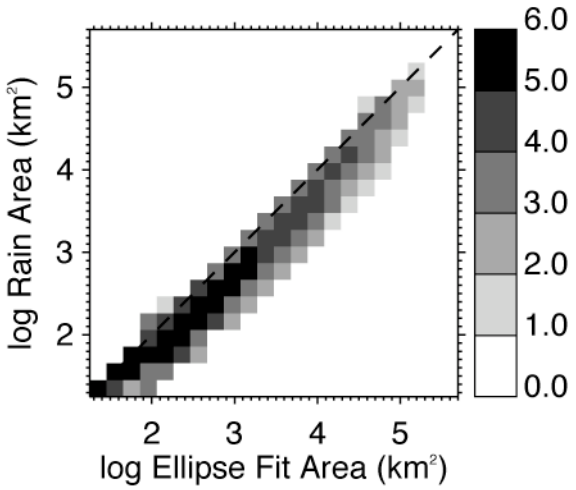

Fig. 2. Shaded log-log density plot of feature rain area versus ellipse fit area.

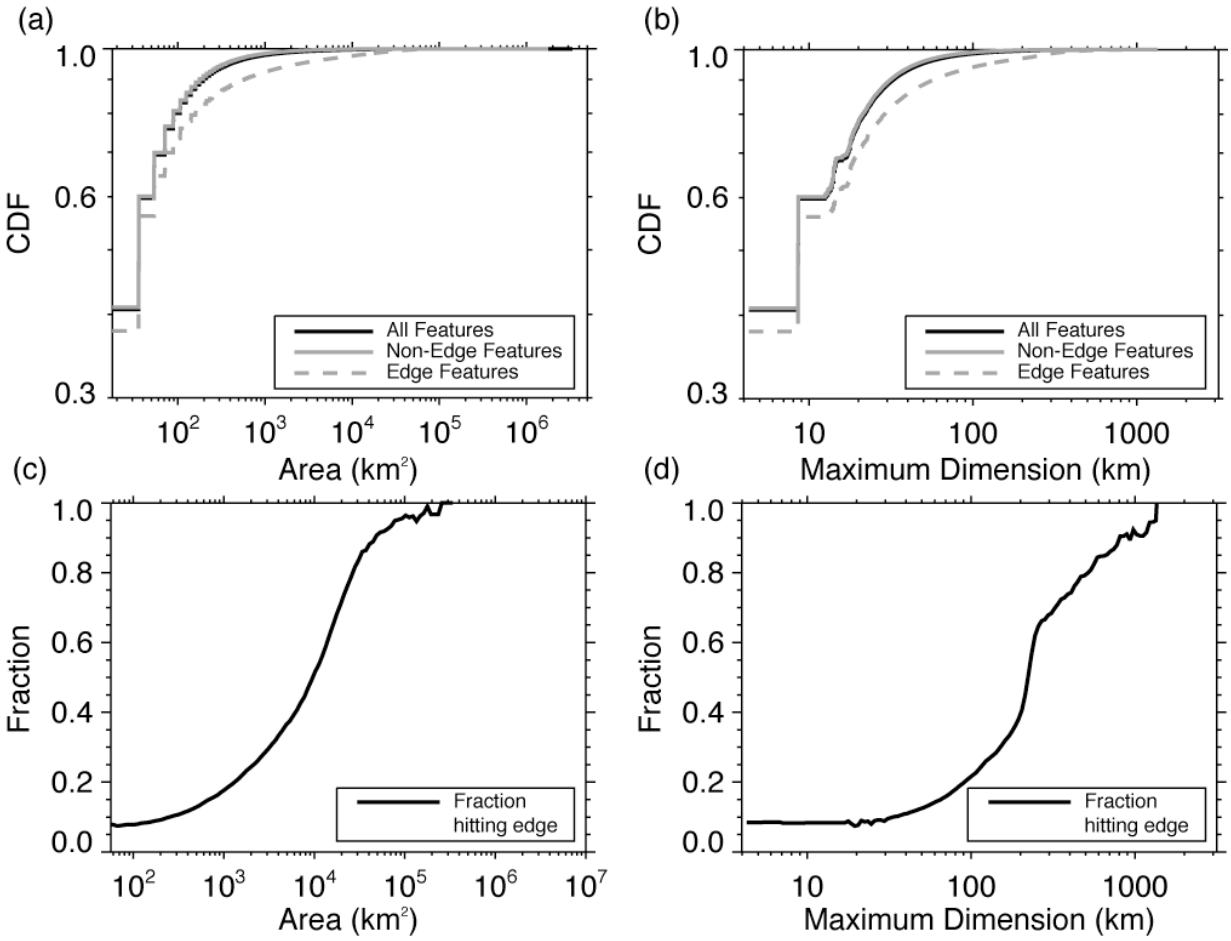

Fig. 3. CDFs of (a) feature area and (b) FMD for all features (dark solid lines), non-edge features (grey solid lines), and edge features (dashed grey lines). Lower plots show the relative fraction of features intersecting the PR swath boundary as a function of feature area (c) and maximum dimension (d).

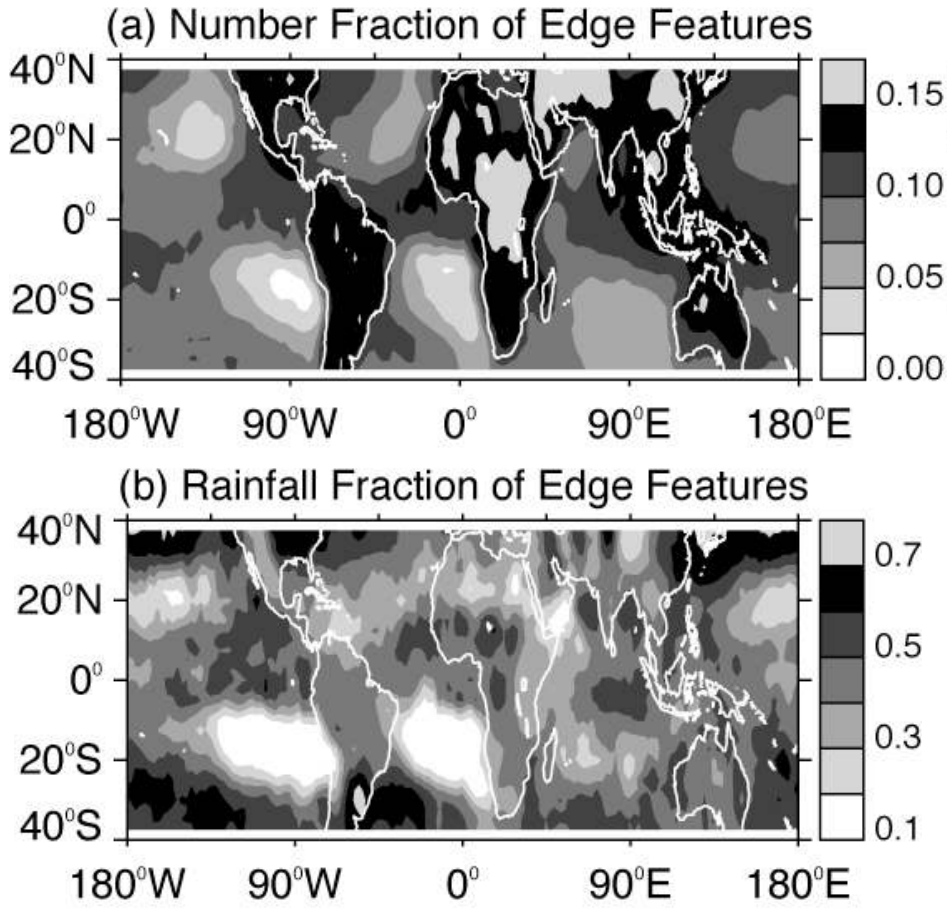

Fig. 4. Contour maps of: (a) the number fraction of edge features (b) the rainfall fraction of edge features.

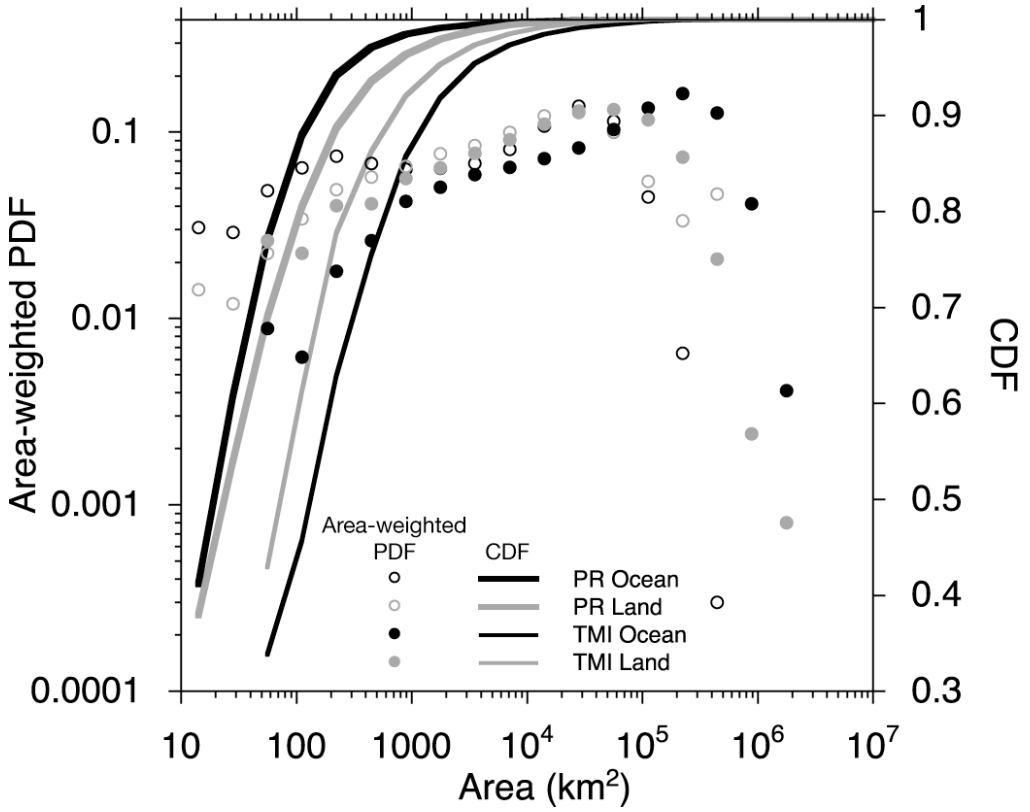

Fig. 5. Fraction of features within each area bin (dots) and CDFs of feature area (lines) for the TMI PFs (filled dots, thin lines) and PR PFs (open circles, thick lines) over ocean (black lines and symbols) and land (grey lines and symbols). The bins range from 1 to 7.3 by 0.3 in log area space.

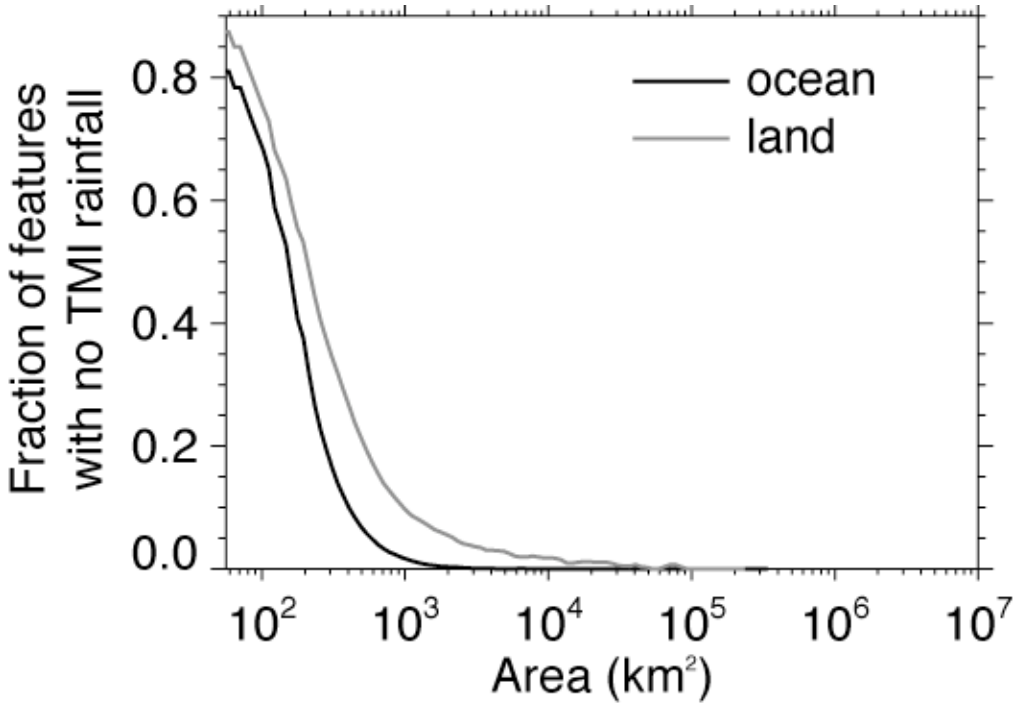

Fig. 6. Fraction of features within each area bin with no TMI rainfall. Bins range from 1.25 to 7 log km^2 by 0.04 log km^2.

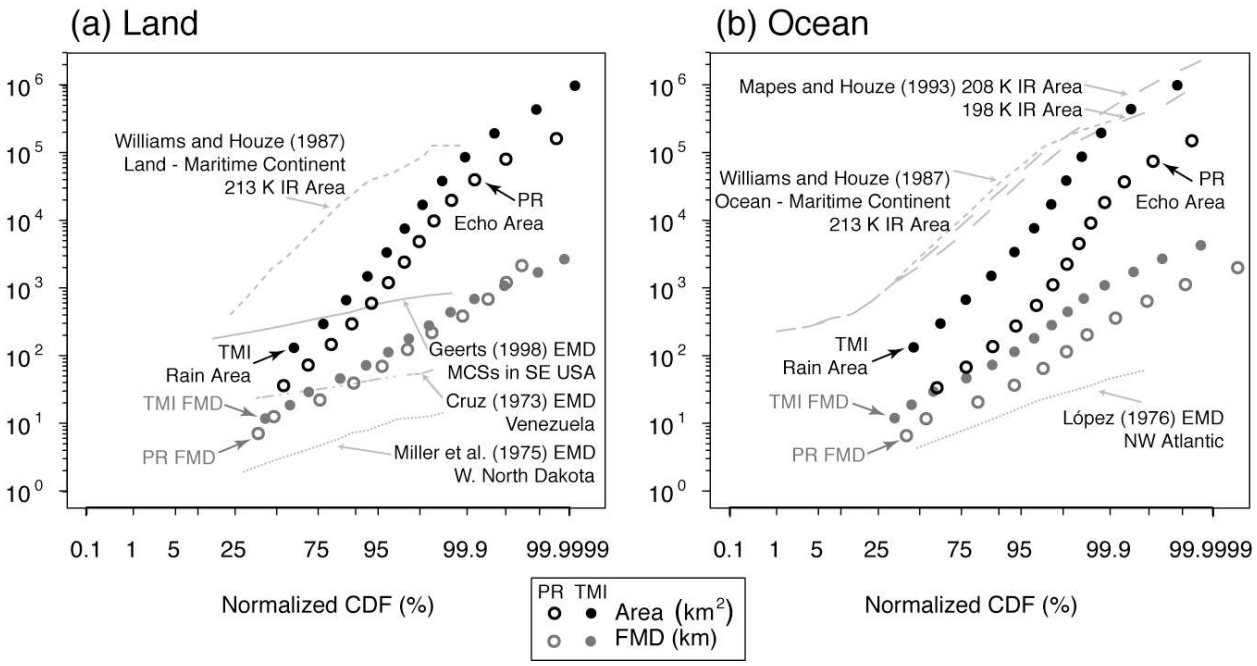

Fig. 7. On a log-probability plot: PR PF (open circles) and TMI PF (filled circles) rain area (black symbols) and FMD (grey symbols) over land (a) and ocean (b). Selected previous studies of IR cloud shield area and radar FMD are overlain. See the text for more details.

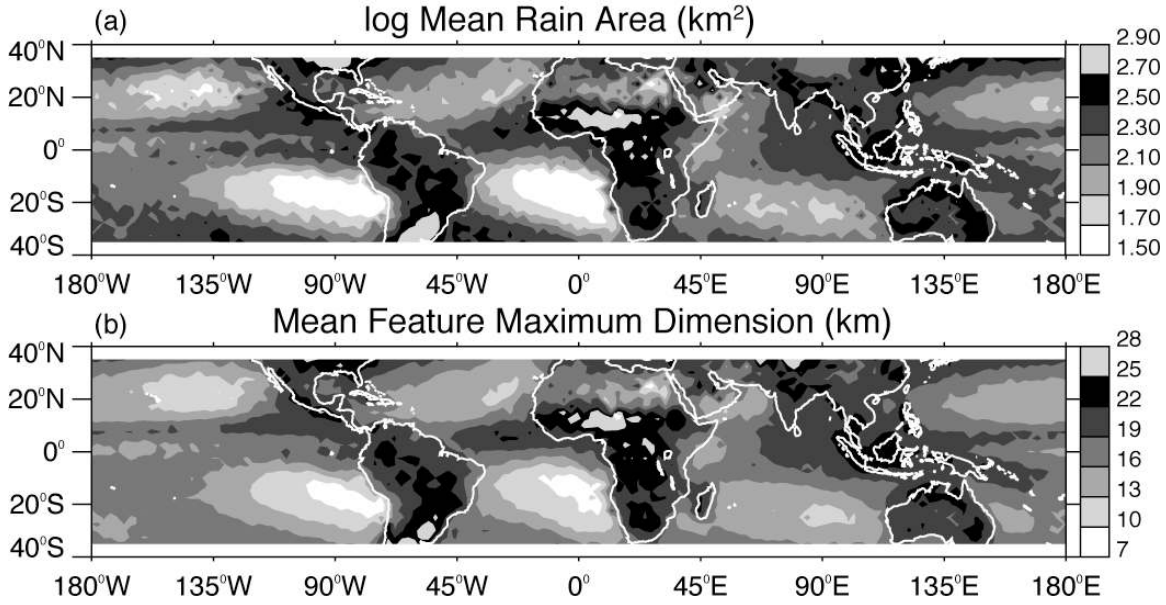

Fig. 8. (a) Log-contour map of mean feature rain area (km^2), (b) contour map of mean feature maximum dimension (km).

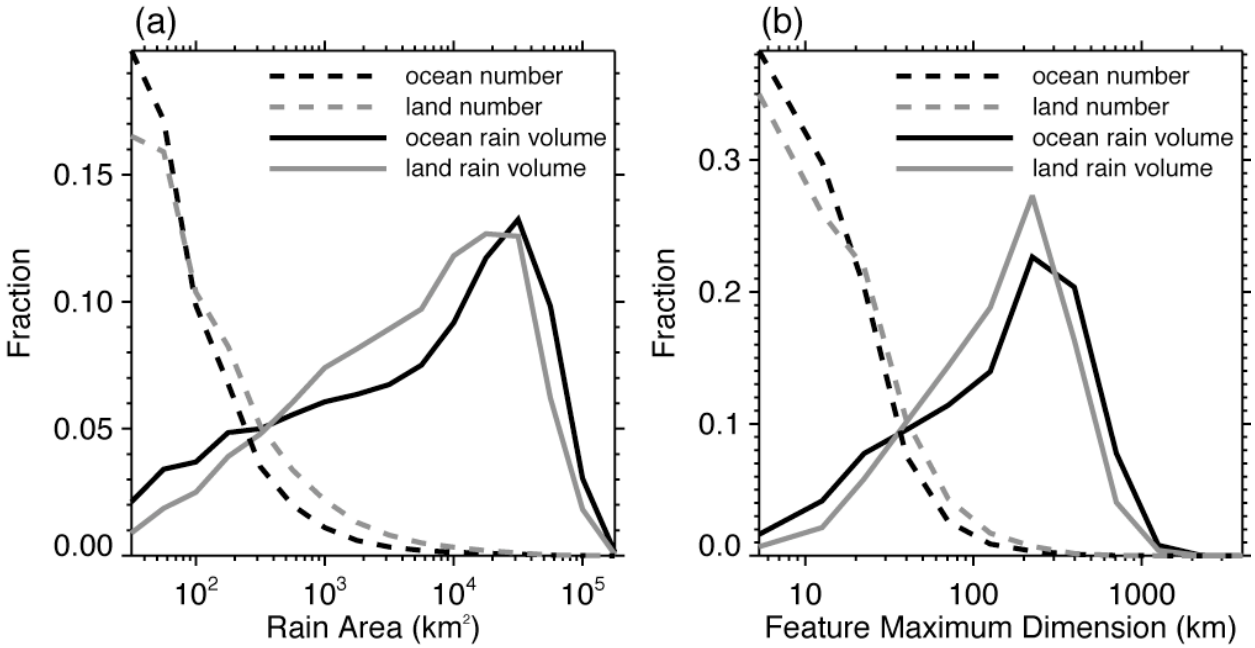

Fig. 9. Number fraction (dashed lines) and rain volume fraction (solid lines) of features over ocean (dark lines) and land (grey lines) as a function of (a) rain area (km^2) and (b) FMD (km). The bins in area range from 1.5 to 5.25 by 0.25 in log km^2 space, while in FMD they range from 0.6 to 3.6 by 0.3 in log km space.

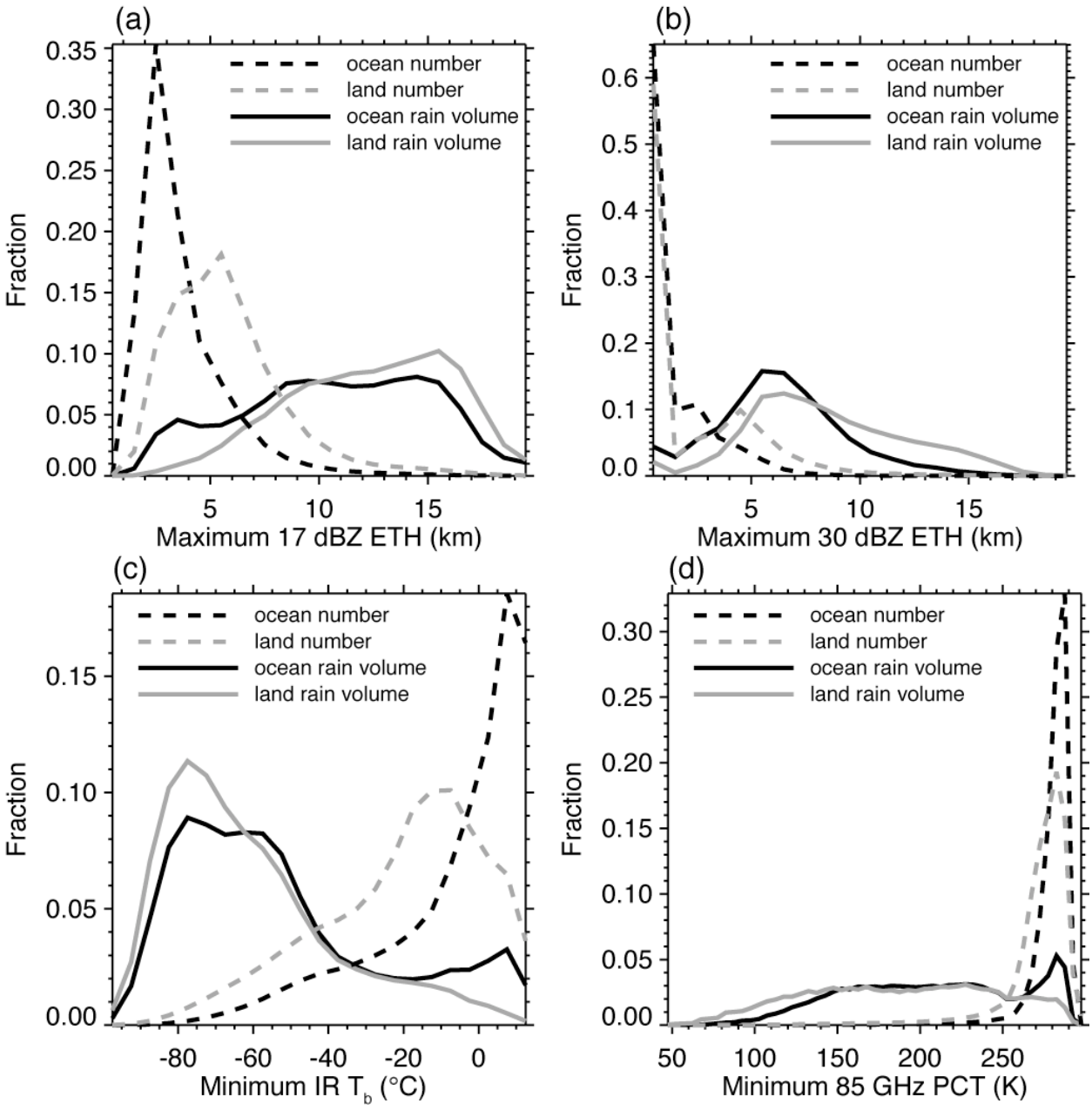

Fig. 10. Number fraction (dashed lines) and rain volume fraction (solid lines) of features over ocean (dark lines) and land (grey lines) as a function of (a) PR maximum 17 dBZ ETH (km), (b) PR maximum 30 dBZ ETH (km), (c) VIRS minimum IR T_b (°C), and (d) TMI minimum 85 GHZ PCT (K). The bins for panels a and b range from 0 to 20 km by 1 km, while for panel c (d) they range from -95 to 15°C by 5°C (45 to 300 K by 5 K).

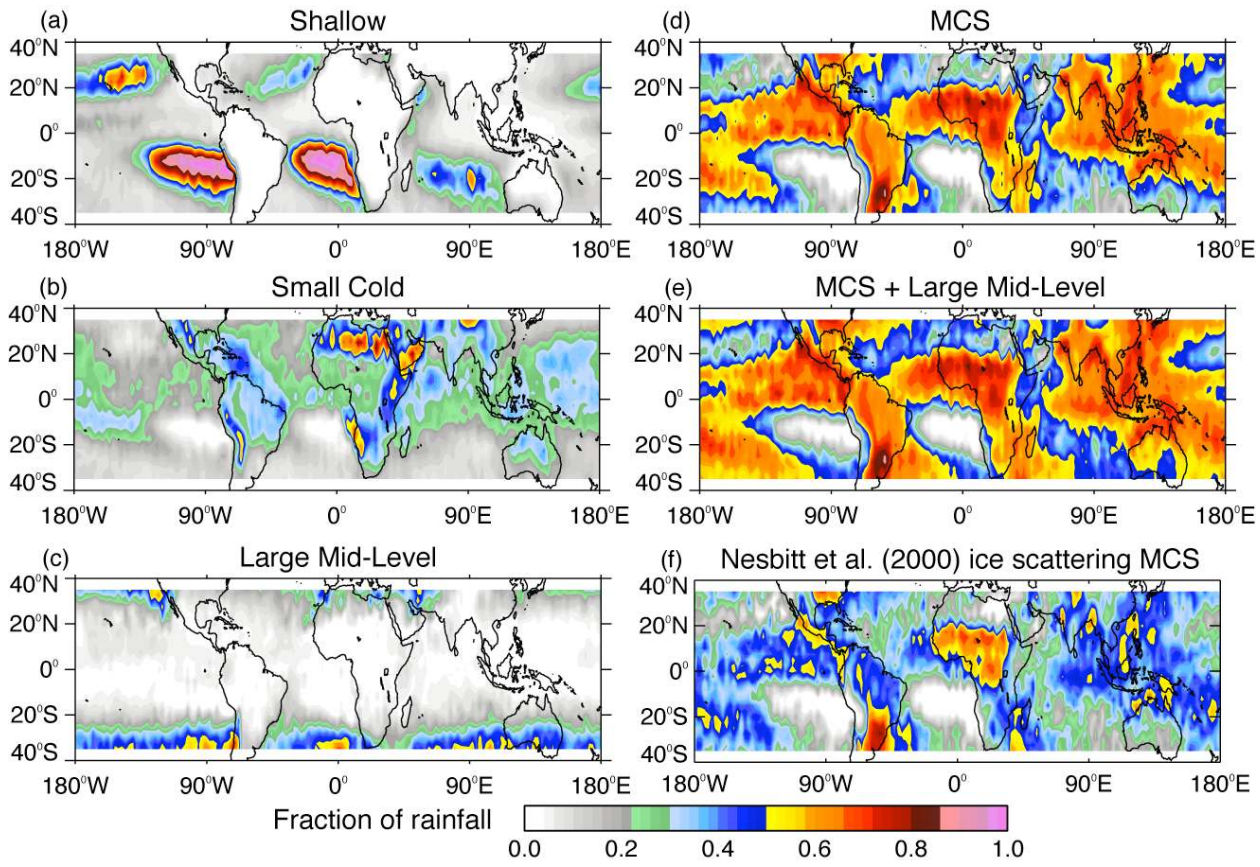

Fig. 11. Shaded contour map of fraction of rainfall by feature type. See text for details.

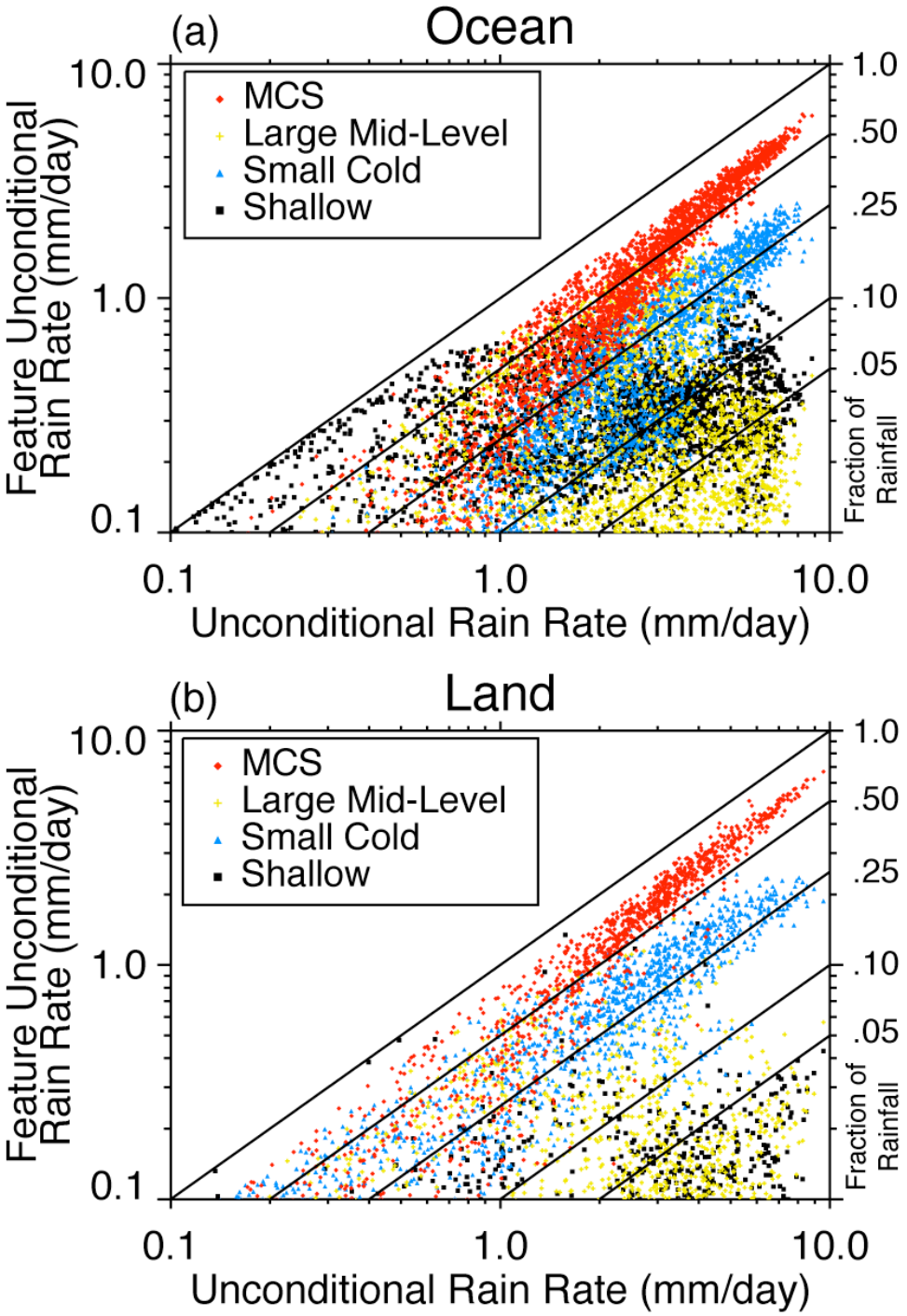

Fig. 12. Scatter diagrams of feature unconditional rain rate (mm dy^{-1}) (see legend at bottom) versus total unconditional rain rate (mm dy^{-1}) in 2.5° grid boxes over ocean (a) and land (b). Fraction of rain contours appear on the diagram as diagonal lines and are labeled at right.

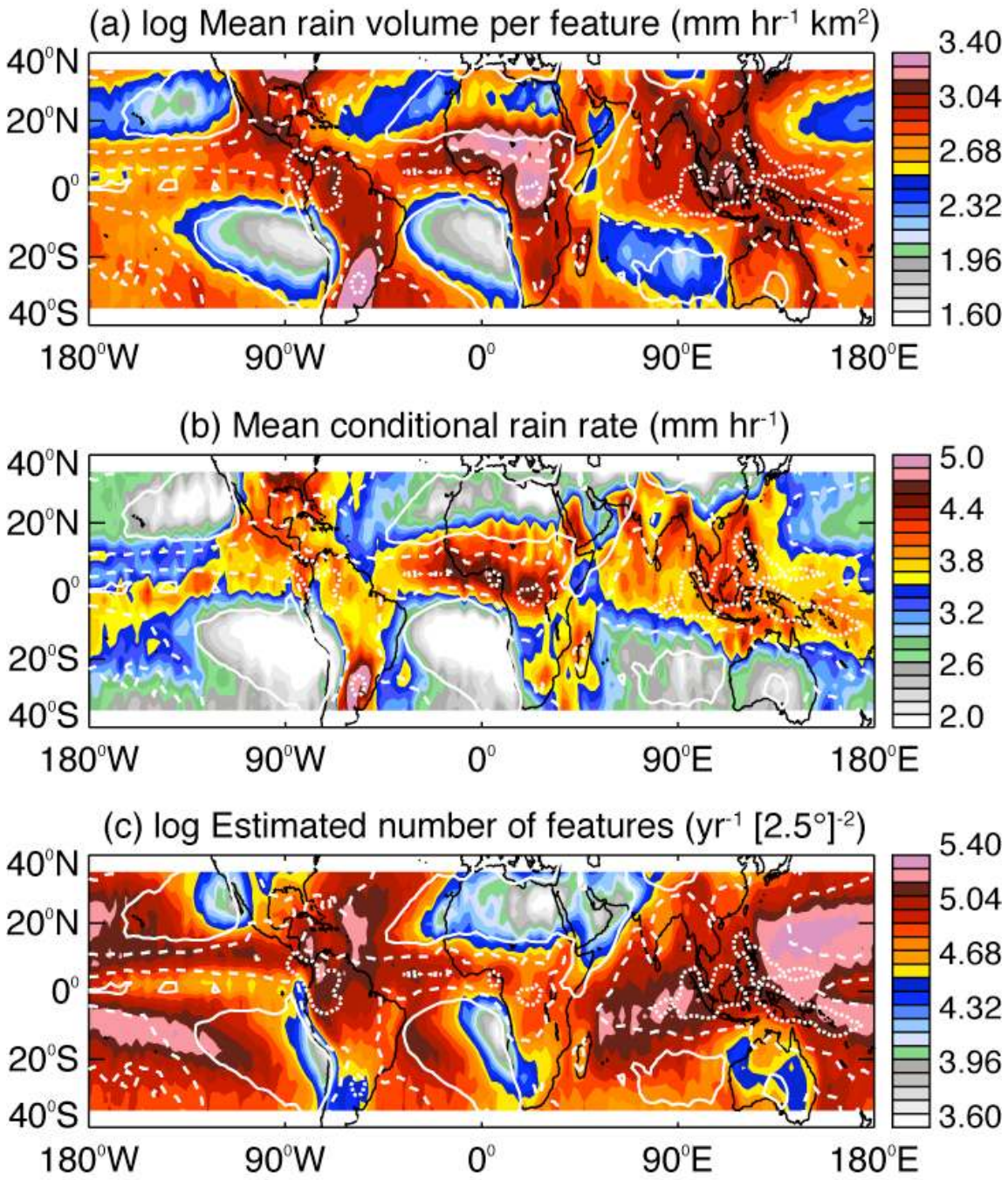

Fig. 13. Shaded contour maps of (a) log mean rain volume per feature (mm hr^{-1} km^2), (b) mean conditional rain rate (mm hr^{-1}), and (c) log estimated number of features per year in each 2.5° box. The 1, 3, and 6 mm dy^{-1} contours of PR unconditional rain rate are shown by the white solid, long, and short dashed lines, respectively.